Hindawi
Geofluids
Volume 2018, Article ID 8532840, 15 pages
https://doi.org/10.1155/2018/8532840

Research Article

Hydrochemical Characteristics and Evolution of Geothermal Fluids in the Chabu High-Temperature Geothermal System, Southern Tibet

X. Wang,[1] G. L. Wang,[1] H. N. Gan,[1] Z. Liu,[2] and D. W. Nan[3]

[1]*Institute of Hydrogeology and Environmental Geology, Chinese Academy of Geological Sciences, Shijiazhuang, Hebei 050061, China*
[2]*School of Water Resources and Environment, Hebei GEO University, Shijiazhuang, Hebei 050031, China*
[3]*The Geothermal Geological Team of Tibet, Tibet Bureau of Exploration & Development of Geology and Mineral Resources, Lhasa 850032, China*

Correspondence should be addressed to G. L. Wang; guilingw@yeah.net

Received 28 October 2017; Revised 29 January 2018; Accepted 18 February 2018; Published 21 March 2018

Academic Editor: Ming Zhang

This study defines reasonable reservoir temperatures and cooling processes of subsurface geothermal fluids in the Chabu high-temperature geothermal system. This system lies in the south-central part of the Shenzha-Xietongmen hydrothermal active belt and develops an extensive sinter platform with various and intense hydrothermal manifestations. All the geothermal spring samples collected systematically from the sinter platform are divided into three groups by cluster analysis of major elements. Samples of group 1 and group 3 are distributed in the central part and northern periphery of the sinter platform, respectively, while samples of group 2 are scattered in the transitional zone between groups 1 and 3. The hydrochemical characteristics show that the geothermal waters of the research area have generally mixed with shallow cooler waters in reservoirs. The reasonable reservoir temperatures and the mixing processes of the subsurface geothermal fluids could be speculated by combining the hydrochemical characteristics of geothermal springs, calculated results of the chemical geothermometers, and silica-enthalpy mixing models. Contour maps are applied to measured emerging temperatures, mass flow rates, total dissolved solids of spring samples, and reasonable subsurface temperatures. They indicate that the major cooling processes of the subsurface geothermal fluids gradually transform from adiabatic boiling to conduction from the central part to the peripheral belt. The geothermal reservoir temperatures also show an increasing trend. The point with the highest reservoir temperature (256°C) appears in the east-central part of the research area, which might be the main up-flow zone. The cooling processes of the subsurface geothermal fluids in the research area can be shown on an enthalpy-chloride plot. The deep parent fluid for the Chabu geothermal field has a Cl^- concentration of 290 mg/L and an enthalpy of 1550 J/g (with a water temperature of 369°C).

1. Introduction

As a part of the Mediterranean-Himalayan geothermal belt, Tibet has abundant geothermal resources. There are a series of S-N-trending normal faults distributed in the Tibetan Plateau, which are the result of the collision between the India and Eurasian plates [1]. These S-N-trending normal fault systems crosscut the Yarlung Zangbo River and Pangong Tso-Nu River suture belts, forming the famous hydrothermal active belt of the Tibetan Plateau [2, 3]. From west to east, there are four major hydrothermally active belts: Tangrayumco-Gucuo, Shenzha-Xietongmen, Yadong-Gulu, and Sangri-Cuona (Figure 1). Yadong-Gulu is the most active hydrothermal belt and has the most concentrated geothermal reserves, followed by the Shenzha-Xietongmen hydrothermal belt. The Chabu high-temperature geothermal system lies in the south-central part of the Shenzha-Xietongmen hydrothermally active belt and has developed an extensive sinter platform with various and intense hydrothermal manifestations.

The heat source for the high-temperature geothermal system in the research area is a partially melted crustal layer, as is seen in most high-temperature geothermal fields [4–14]. A high-temperature geothermal system with a magmatic

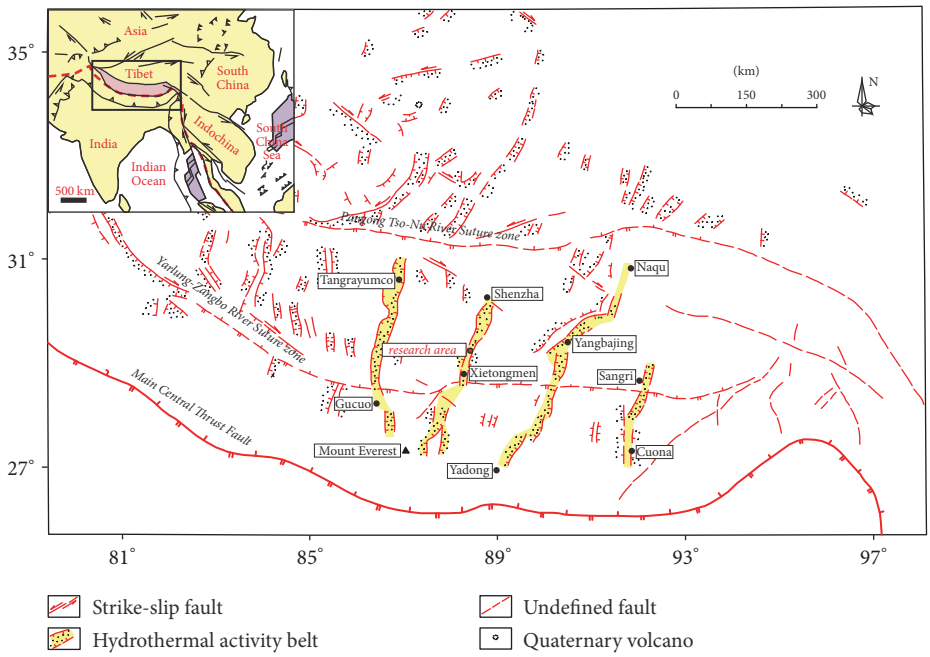

FIGURE 1: Distribution of hydrothermally active belts on the Tibetan Plateau [22–24].

heat source usually hosts deep parent fluids that remain in equilibrium with the surrounding rock. The pH of these fluids is near neutral; the principal anion and cation are Cl^- and Na^+, respectively [15–17]. This type of deep geothermal fluid ascending in a geothermal system may cool by (1) conduction of heat to the surrounding rock, (2) adiabatic boiling, (3) mixing with cooler water, or (4) a combination of these [18–21].

Except for some fundamental geological investigations (stratum, structure, and magmatite) and some preliminary resource assessment, there are very few studies on this research area, especially on the hydrochemical characteristics, temperatures, and cooling processes of geothermal fluids. Thus, the aim of this work is to fill this gap by combining the hydrochemical characteristics of hot spring waters with cluster analysis, chemical geothermometers, and mixing models (silica-enthalpy and enthalpy-chloride). This work could provide valuable guidance for further assessment, exploitation, and utilization of geothermal resources of the Chabu geothermal field.

2. Geological Setting

The research area lies in the Lhasa–Gangdise block between the Yarlung Zangbo River suture belt and the Pangong Tso-Nu River suture belt and is largely bounded by the Pangong Tso-Nu River deep fracture in the north and Yaluzangbu River deep fracture in the south, both of which trend approximately E–W. Extension fractures are well developed in the research area, and the major faults extend in S–N and SW–NE directions forming the main heat-controlling structures.

The strata exposed in the research area are Paleogene and Quaternary units. Paleogene rocks are mainly lithic tuff and are distributed to the south of the research area and appear as strip belts along a NE or NW direction. Quaternary unconsolidated sediments are found throughout the area. Quaternary sinters are distributed in the central part of the Chabu geothermal field and are mainly composed of siliceous minerals. The sinter platform contains approximately 80 thermal springs and imbricated deposits from NE to SW.

The magmatic rocks exposed in the research area are primarily biotite alkali-feldspar granite and biotite granite of Paleogene age, as well as porphyritic biotite monzonitic granite and two-mica adamellite of Neogene age (Figure 2).

3. Materials and Methods

In this study, 36 geothermal spring samples are collected systematically from the north-central part of the sinter platform which holds the most concentrated and intense hydrothermal manifestations (Figure 3). Table 1 includes the sample ID, concentration of major ions and some trace ions, measured emerging temperatures, mass flow rates, and charge imbalance for all the geothermal spring samples.

The temperature (T) and pH values of the geothermal water samples were measured with hand-held meters on-site prior to sampling. All geothermal water samples were filtered through 0.45 μm membranes and stored in three 200 mL polyethylene bottles that had been rinsed with water from the sample source twice before sample collection. For SiO_2 analyses, the geothermal water samples were diluted to 10% of their initial concentration using deionized water. For metallic and cation element analyses, samples were acidified with HNO_3 to pH 1. No reagents were added to the samples for inorganic anion analysis. All water samples were analyzed at the Key Laboratory for Groundwater Science and Engineering of the Ministry of Land and Resources with the Determination Method for Underground Water published by

Table 1: Hydrochemical characteristics of geothermal spring samples from the research area (in mg/L, except for pH in standard pH units, mass flow rate in L/min, T in °C, and charge imbalance in %). Sample H1 is the cold groundwater of the research area. The samples are listed in the order of the results of cluster analysis mentioned in "Cluster Analysis."

Group	Sample ID	T	Mass flow rate	pH	TDS	K	Na	Ca	Mg	Cl	SO_4	HCO_3	CO_3	Li	F	SiO_2	B	Charge imbalance	Hydrochemical type
	H1	11	-	7.34	62.35	1.02	3.27	8.61	0.69	0.68	0.74	37.7	0	0.0098	0.31	13.79	0.022	−0.96	Ca-Na-HCO_3
	C31	87.3	1842.6	8.4	1933.04	52.38	403.14	2.47	3.25	303.18	89.96	478.71	60.99	7.83	11	309.58	48.84	−1.18	Na-Cl-HCO_3
	C34	87.2	1311.6	8.42	1731.81	47.48	382.1	1.65	5.5	282.08	98.85	513.44	35.37	7.92	10	143.82	47.92	−1.58	Na-Cl-HCO_3
	C35	78.6	70.3	8.6	1648.91	46.28	371.32	1.65	3.5	277.85	92.92	453.91	51.23	7.98	9.9	123.74	47.46	−1.53	Na-Cl-HCO_3
	C6	81.4	172.8	8.64	1832.81	47.54	385.2	2.42	1.96	281.08	99.54	458.34	53.18	8.37	9.8	294.12	47.46	−0.87	Na-Cl-HCO_3
	C32	87	98.2	8.82	1784.5	48.08	391.2	1.24	4	287.7	97.86	410.5	90.26	7.92	10.4	287.84	47.96	−1.64	Na-Cl-HCO_3
1	C3	80.8	21.6	8.73	1691.54	46.4	385.2	2.42	2.45	286.02	103.4	406.84	83.57	8.95	9.84	162.32	48.38	−1.61	Na-Cl-HCO_3
	C33	87.3	17.3	8.9	1593.57	44.56	378.25	1.65	4.5	279.97	92.92	311.29	129.29	7.38	9.5	135.06	47.54	−1.63	Na-Cl-HCO_3
	C5	81.8	151.2	8.82	1769.56	43.2	379.5	2.42	3.91	276.84	89.87	375.94	98.76	8.21	9.62	289.94	47.46	−1.03	Na-Cl-HCO_3
	C19	78.7	324.0	8.51	1800.12	53.22	378.25	1.61	0.98	282.49	76.34	388.81	96.23	7.47	9.82	312.14	48.38	−1.56	Na-Cl-HCO_3
	C20	83.2	496.8	8.55	1854.85	58.62	384.94	1.61	1.47	286.73	78.28	435.16	73.44	8.13	10	321.9	48.38	−0.53	Na-HCO_3-Cl
	C18	79.2	64.8	8.48	1848.79	58.94	397.98	1.61	0.98	284.61	74.41	383.66	96.23	7.96	9.43	345.36	46.54	1.4	Na-Cl-HCO_3
	C1	70.4	6.5	8.25	1850.07	41.68	420	4.83	1.96	292.38	89.87	538.15	43.05	8.37	10	153.6	49.30	0.1	Na-Cl-HCO_3
	C26	76	0.0	8.21	1864.55	39.58	393.6	4.84	2.45	282.49	86.01	533.01	20.25	7.89	10.2	296.22	46.54	0.01	Na-HCO_3-Cl
	C23	81.6	0.0	8.25	1923.22	39.78	407.36	4.03	2.45	290.96	78.28	517.56	45.58	8.41	10.4	305.64	52.99	−0.09	Na-HCO_3-Cl
	C36	77.6	432.0	8.22	1798.58	39.43	397.94	4.03	1.47	278.25	76.34	468.63	53.18	8.14	9.06	270.64	49.30	1.13	Na-HCO_3-Cl
2-1	C11	80.6	216.0	8.24	1843.16	41.2	396.54	4.03	1.47	279.66	72.48	509.83	40.52	8.24	9.9	284.64	48.38	0.47	Na-HCO_3-Cl
	C25	77.2	43.2	8.22	1894.08	48.42	407.08	6.45	1.96	281.08	89.87	538.16	22.79	8.11	10.4	285.6	48.38	1.65	Na-Cl-HCO_3
	C4	72.2	0.2	8.6	1702.44	44.96	385.4	2.42	2.93	276.84	86.01	489.23	37.99	7.98	9.44	174.18	45.61	0.11	Na-HCO_3-Cl
	C21	77.4	43.2	8.34	1796.67	43.2	395.86	6.45	0.98	269.07	87.94	471.21	45.58	8.18	9.22	275.18	45.61	1.94	Na-HCO_3-Cl
	C7	80	0.0	8.5	1783.32	46.2	401.29	4.83	1.47	272.6	86.01	435.16	65.84	8.04	9.4	261.4	47.46	1.17	Na-HCO_3-Cl
	C24	66	6.5	7.5	1878.5	39.85	372.36	15.32	2.93	264.83	76.34	605.11	0	7.94	9.3	295.68	46.54	−0.26	Na-HCO_3-Cl
	C28	71	21.6	7.53	1950.27	44.7	400.91	20.97	2.45	278.25	78.28	669.48	0	7.94	9.91	239.22	49.30	0	Na-HCO_3-Cl
	C22	78.8	43.2	8.21	1830.68	44.5	383.68	10.48	1.47	264.13	78.28	592.23	20.25	7.71	9.62	227.74	47.46	0.03	Na-HCO_3-Cl
2-2	C30	57.6	2.2	6.89	1915.04	43.8	397.84	17.74	0.98	280.05	84.07	581.93	0	7.92	9	302.5	46.54	1.17	Na-HCO_3-Cl
	C27	70	0.0	7.38	1929.03	42	390	11.03	2.2	271.9	79.24	569.06	0	7.49	9.96	362.15	47.46	1.74	Na-HCO_3-Cl
	C29	62.6	43.2	7.4	1980.45	37.84	399.6	20.97	2.93	272.6	76.34	623.13	0	7.89	9.42	344.34	45.61	1.93	Na-HCO_3-Cl
	C2	77.6	86.4	8.1	1922.72	40.18	399	11.4	1.47	272.6	70.2	587.08	0	8.11	9.63	328.86	48.38	1.43	Na-HCO_3-Cl
	C14	70	2.2	7.62	1828.63	40.6	387.28	22.58	5.65	272.6	123.69	589.66	0	8.09	10.6	227.13	48.00	0.37	Na-HCO_3-Cl
	C16	66.2	21.6	7.6	1943.51	38.42	397.62	12.9	7.82	272.6	115.96	636	0	7.49	9.8	243.98	49.76	−0.96	Na-HCO_3-Cl
	C15	62	2.2	7.7	1865.26	38.7	355.9	22.58	5.86	254.24	96.63	602.53	0	7.42	9.45	276.96	47.96	−1.05	Na-HCO_3-Cl
	C8	67.8	2.2	7.3	1925.16	37.6	375.98	19.35	10.76	262.72	104.37	641.15	0	7.66	9.43	261.76	47.92	−0.78	Na-HCO_3-Cl
3	C12	68.8	21.6	7.28	1878.22	40.2	384.12	11.29	8.8	268.37	98.57	620.56	0	7.93	10.4	225.94	49.76	−0.43	Na-HCO_3-Cl
	C9	58.8	21.6	6.6	1931.58	39.2	372.1	17.74	7.82	266.95	92.77	610.26	0	7.14	9.8	307.31	49.76	−0.59	Na-HCO_3-Cl
	C17	61.4	21.6	7.17	1914.32	41.5	370.9	11.29	5.86	262.72	104.37	593.52	0	7.78	10.8	312.17	47.92	−1.32	Na-HCO_3-Cl
	C13	74.6	32.4	7.42	1881.16	36.4	377.82	19.35	7.82	266.95	108.23	626.99	0	7.29	10.2	228.16	47.92	−1.41	Na-HCO_3-Cl
	C10	73	0.0	7.18	1965.03	38.2	375.78	16.13	6.85	269.78	105.1	602.53	0	4.12	9.8	325.78	51.60	−1.29	Na-HCO_3-Cl

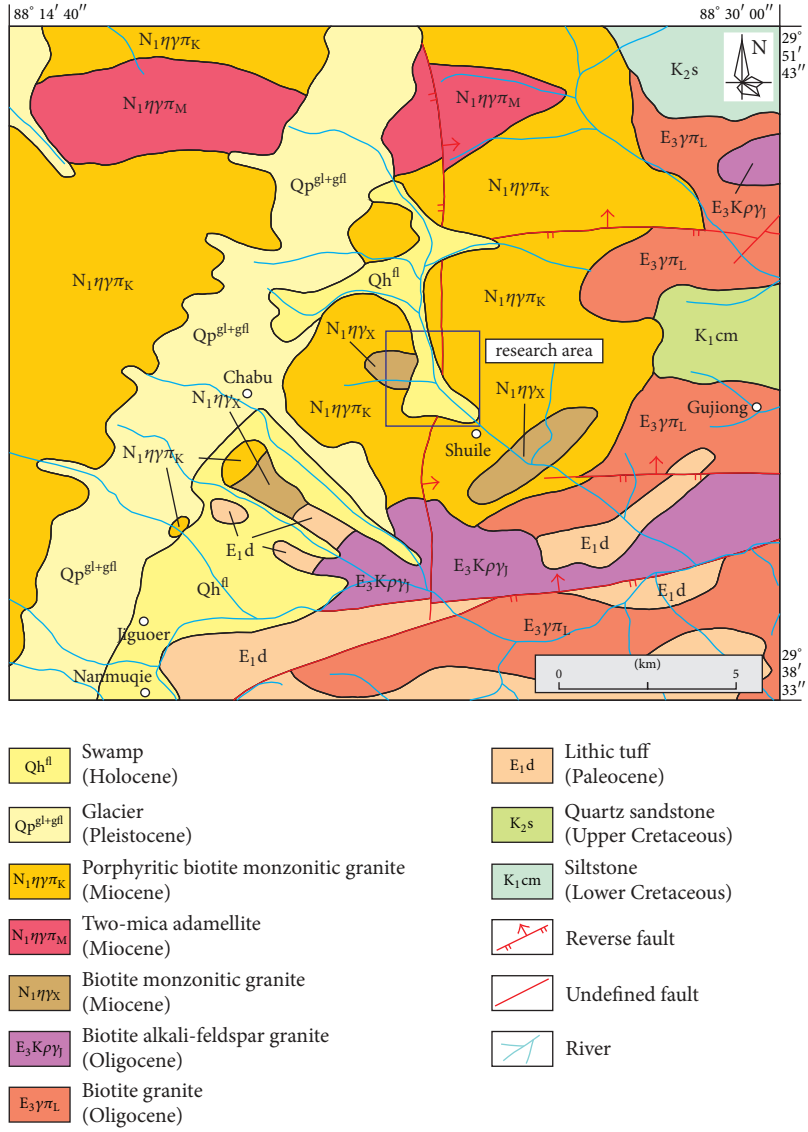

Figure 2: Geological map of the research area.

the Chinese government (DZ/T 0064-1993). The concentrations of major cations and trace elements were detected using inductively coupled plasma atomic emission spectroscopy (ICP-AES) (ICAP-6300) and inductively coupled plasma mass spectrometry (ICP-MS 7500C), respectively, while the concentrations of major anions were measured using ion chromatography (DX-120).

The ion charge imbalances for the water samples were calculated using the program AquaChem, and the results showed that all of the samples have a charge imbalance less than ±5% (Table 1). Values in this range are usually accepted as valid and can support the reliability of the data used in this work [25–27].

In this work, all the samples were divided into three groups by cluster analysis of the major elements; then the hydrochemical characteristics, emerging temperatures, and mass flow rate of each group were compared. The temperatures of the geothermal reservoirs were estimated using silica and cation geothermometers, and the optimum temperature of each sample was selected by taking into account the measured emerging temperature and the mass flow rate of the corresponding spring. To verify the reliability of the chemical geothermometers, the silica-enthalpy mixing models were applied to estimate the geothermal reservoir temperatures and identify mixing processes. The varying pattern of geothermal reservoir temperatures was explored and the major ascending zone was delineated using contour maps. Based on the aforementioned work, different cooling processes of ascending geothermal fluids were speculated, and the temperature of the deep parent fluid was estimated by integrating the hydrochemical characteristics with an enthalpy-chloride graph. The methodologies of the main methods and models applied in this work are described as follows.

Table 2: Calculation formulas of chemical geothermometers used in this work.

Geothermometer	Calculation formula	Reference
Chalcedony (no loss of steam)	$t = 1032/(4.69 - \log SiO_2) - 273.15$	Fournier (1977)
Chalcedony (maximum steam loss)	$t = 1264/(5.31 - \log SiO_2) - 273.15$	
Quartz (no loss of steam)	$t = 1309/(5.19 - \log SiO_2) - 273.15$	
Quartz (maximum steam loss)	$t = 1522/(5.75 - \log SiO_2) - 273.15$	
Na-K-Ca	$t = 1647/(\log(Na/K)+\beta(\log(\sqrt{Ca}/Na)+2.06)+2.47)-273.15$ $\beta = 4/3$ (when $t < 100^\circ C$) or $\beta = 1/3$ (when $t > 100^\circ C$)	Fournier (1981)
Na/K	$t = 1217/(\log(Na/K) + 1.483) - 273.15$	
K/Mg	$t = 4410/(13.95 - \log(K^2/Mg)) - 273.15$	Giggenbach (1988)

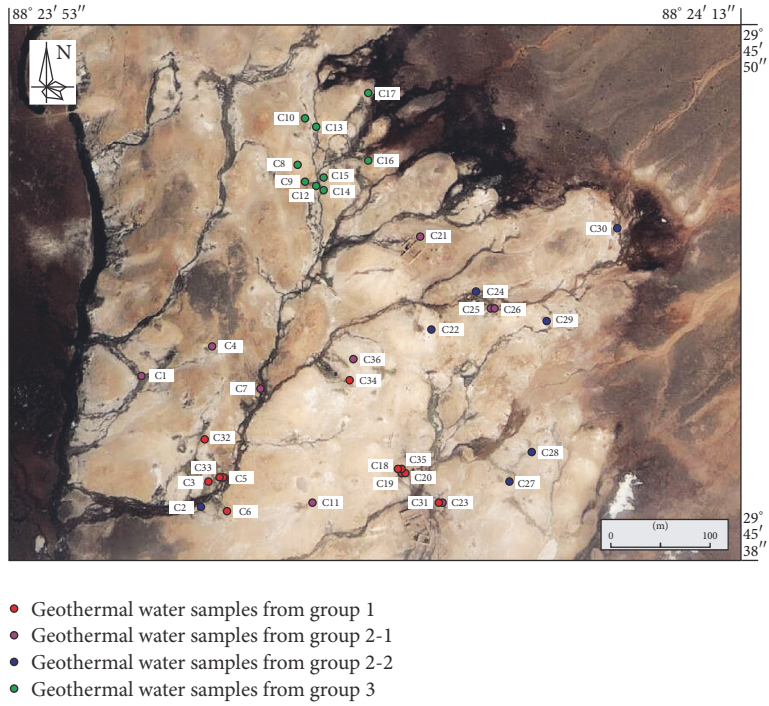

Figure 3: Sampling locations in the research area. The samples are colored according to the results of cluster analysis mentioned in "Cluster Analysis."

3.1. Cluster Analysis. As one of the multivariate statistical methods, cluster analysis (CA) is a convenient and effective means to explore geochemical patterns and interpret hydrochemical characteristics [28]. Cluster analysis was used as an analysis of variance approach (hierarchical cluster) to measure the distance between variable clusters, attempting to minimize the sum of squares of any two clusters that could be formed at each step (square euclidean distance) [29]. Hydrochemical data with similar properties were clustered in a group. In this study, the contents of the major elements, including K, Na, Ca, Mg, Cl, SO_4, HCO_3, and CO_3, were considered to evaluate the characteristics of the geothermal spring samples using the average linkage hierarchical method, which is designed to optimize the minimum variance within groups. The similarities among samples were measured using the squared euclidean distance method [30]. To avoid misclassifications arising from the different orders of magnitude of the variables, the variances for each variable were sourced from a previous study [31, 32].

3.2. Chemical Geothermometer. Chemical geothermometers were applied to estimate the temperatures of the geothermal reservoirs, including a silica geothermometer (the solubility of silica changes as a function of temperature and pressure) and a cation geothermometer (the equilibrium constants for exchange and alteration reactions are temperature-dependent). The formulas for the calculations used in this research are listed in Table 2.

3.3. Mixing Models. The silica-enthalpy mixing model was applied in this research to estimate the temperatures of geothermal reservoirs and identify mixing processes [19, 33, 34]. In this model, enthalpy is used as a coordinate rather than a temperature, because the combined heat contents of

two waters at different temperatures are conserved when the waters are mixed, but the combined temperatures are not [35]. In the silica-enthalpy model, the silica concentrations of the analyzed samples are plotted against their corresponding on-site enthalpies. The enthalpy values are determined using international steam tables [36]. For application to emerging geothermal samples, two end-member fluids were considered: a cold groundwater sample and an initial deep geothermal water. The point of the initial deep geothermal water can be obtained using two different methods. For the situation in which no steam is lost before mixing, one plots the silica and heat contents (enthalpies) of the cold and emerging spring waters as two points and then draws a straight line through these points to intersect the quartz solubility curve; intersection A_1 then provides the original silica content and enthalpy of the deep hot water. For the situation in which the maximum amount of steam is lost from the hot water before mixing, one plots the silica and heat contents of the cold and emerging spring waters as two points, draws a straight line through the points, and extends that line to intersect the vertical line from the enthalpy values of 419 J/g (corresponding to 100°C, the boiling point of water) and subsequently from this intersection point moves horizontally to the maximum steam loss curve and then moves vertically to intersect the quartz solubility curve. The original silica content and enthalpy of the deep hot-water component are provided by point A_2 [18].

The enthalpy-chloride model was first proposed by [19] to describe the cooling processes of geothermal fluids during ascent and to estimate the temperature and Cl^- concentration of the deep parent fluid. As in the silica-enthalpy mixing model, in this model enthalpy is also used as a coordinate rather than a temperature. In brief, the Cl^- concentrations of the cold water, steam, and emerging spring waters can be plotted against their corresponding on-site enthalpies. Lines from the emerging spring waters towards the steam point represent the variation in enthalpy and Cl^- content of the liquid water fraction caused by the process of steam separation during passage to the surface. Lines from the emerging spring waters towards the cold water represent the variation in enthalpy and Cl^- content caused by mixing with shallow colder waters during ascent. For samples that are mainly cooled by conduction during ascent, their chloride contents generally will be nearly the same as those of waters from aquifers feeding the springs. By combining the cooling processes of the subsurface geothermal fluids and the reasonable reservoir temperatures, the temperature and salinity of the deep parent fluid can be predicted.

4. Results and Discussion

4.1. Hydrochemical Characteristics

4.1.1. Cluster Analysis. The dendrogram constructed by the software SPSS17.0 shows that all the geothermal samples are divided into three clusters, groups 1, 2, and 3, and group 2 can be further divided into two subclusters (Figure 4). From the sampling location map (Figure 3), it can be seen that the samples of group 1 and group 3 are distributed

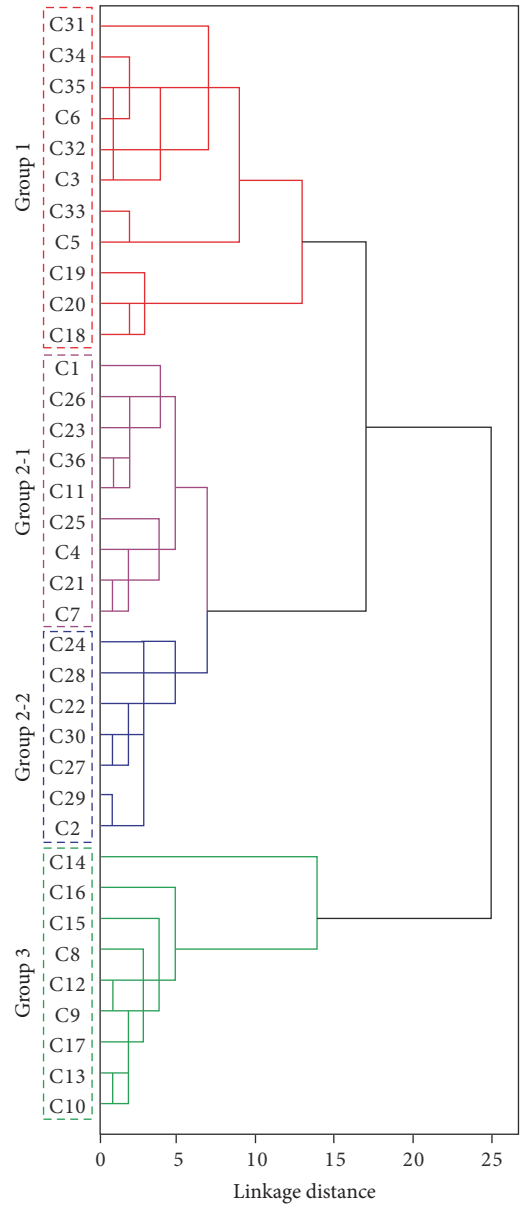

Figure 4: Dendrogram showing the results of the cluster analysis performed on the geothermal spring samples from the research area.

in the central part and northern periphery of the sinter platform, respectively. Samples of group 2 are scattered in the transitional zone between groups 1 and 3, with subgroup 2-1 distributed closer to the central part, where its hydrochemical characteristics are more similar to those of group 1.

4.1.2. Indicative Significance of Geothermal Fluid Composition. The hydrochemical characteristics of all water samples are summarized in Table 1. Cold groundwater in the research area is of the HCO_3-Ca-Na type. All the geothermal spring samples contain Na^+ as the predominant cation, while the proportions of Na^+ contents decrease from groups 1, 2, and 3 to the ambient cold groundwater. The predominant anions of the geothermal spring samples from different groups

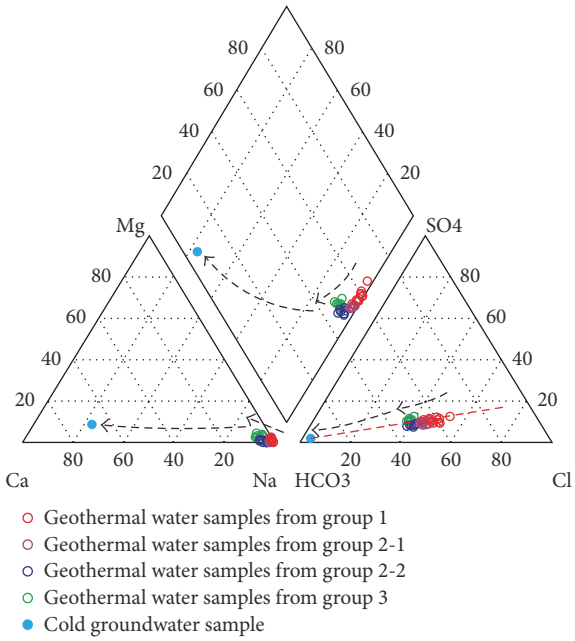

Figure 5: Piper diagram of geothermal spring samples in the research area.

differ from each other. Samples of group 1 contain Cl^- and HCO_3^- as the predominant and subordinate anions, while the opposite is found in group 3. As the transitional group between groups 1 and 3, most samples of group 2 contain HCO_3^- as the predominant anion and Cl^- as the subordinate anion (Figure 5).

On the triangular plot of Cl-SO_4-HCO_3 + CO_3 (Figure 5) and the Na-K-Mg diagram (Figure 6), a linear relationship of all the samples is presented and was found to be one main indicator of mixing between geothermal fluids and shallow cooler waters. Furthermore, samples of groups 1, 2, and 3 draw near to cold groundwater, indicating that there is a gradually increasing mixture of geothermal waters and cooler shallow water from group 1 to group 2 to group 3.

Figure 6 shows that almost all the samples can be classified as immature waters. According to [15], high-temperature well discharges plot on the full equilibrium line and somewhat above actually measured deep temperatures, while the associated spring waters are off the full equilibrium line and shift to lower temperatures in the Na-K-Mg diagram. This indicates acquisition of Mg by spring waters in response to decreasing temperatures is faster than that of Na. Therefore, on the premise of insufficient information, calculation results of geothermal spring samples based on the Na-K-Mg system still bear a certain significance.

4.2. Temperatures of Geothermal Reservoirs

4.2.1. Geothermometric Applications. The temperatures of the geothermal reservoirs were estimated using a silica geothermometer [18], Na-K-Ca and Na/K geothermometers [37], and K/Mg geothermometer [15]. The calculation results are listed in Table 3.

4.2.2. Quartz Geothermometer. Silica geothermometers contain quartz and chalcedony geothermometers which are based on the solubility of silica changing as a function of temperature and pressure. The quartz geothermometer is more applicable than is the chalcedony geothermometer in the research area because quartz controls the dissolved silica concentration at temperatures higher than 150°C [18, 38, 39], which is the case in the research area where all of the quartz results and most of the chalcedony results are above 150°C. Therefore, the calculation results of the quartz geothermometer are adopted in this research.

The temperatures of the geothermal reservoirs estimated using the quartz geothermometer were selected for the optimum temperature of each sample (i.e., the calculated temperatures were chosen between the values of the maximum steam loss and no loss of steam) taking into account the measured emerging temperature and the mass flow rate of the corresponding spring [40]. Waters that flow at relatively large mass rates directly to the surface will cool adiabatically, and the emerging spring water will be at or slightly above the boiling temperature for the prevailing atmospheric pressure [41]. For these waters, the quartz geothermometer with the maximum steam loss was applied. Boiling generally occurs when the water temperatures reach 80°C at high altitudes in the research area [42, 43], and, following [44], 30 L/min is subjectively considered as a large mass flow rate for the spring systems. For the geothermal spring samples, of which the emerging temperatures are above 70°C and the mass flow rates are higher than 30 L/min, the calculated results from the quartz geothermometer with maximum steam loss were adopted. Otherwise, the calculated results from the quartz geothermometer with no loss of steam were adopted, as waters that flow to the surface at relatively slow rates of mass movement and that show emerging spring temperatures much lower than the maximum temperature in the convecting hydrothermal system are generally cooled by conduction. The high mass flow rates usually keep pace with the high emerging temperatures; therefore, for a small part of samples that lack mass flow rate data, the optimum temperatures were only selected by the measured emerging temperature. The optimum temperature of each spring sample selected from the quartz geothermometers is in bold font in Table 3. The adoption rates of the results from the quartz geothermometer with maximum steam loss gradually decreased from group 1 to group 3.

4.2.3. Cation Geothermometer. The Na-K-Ca, Na/K, and K/Mg geothermometers were also used to estimate geothermal reservoir temperatures. When the Na-K-Ca geothermometer is used to estimate subsurface temperatures, $\log(\sqrt{Ca}/Na)$ first needs to be calculated. When all the results from the water samples are negative, geothermal reservoir temperatures can be calculated using the β value of 1/3 [45]. These results are listed in Table 3.

For the samples of group 1, the results from the Na/K geothermometer are consistent with those from the Na-K-Ca geothermometer, as the Ca contents are generally lower than 3 mg/L. For the samples of groups 2 and 3, the results from the Na/K geothermometer are increasingly higher

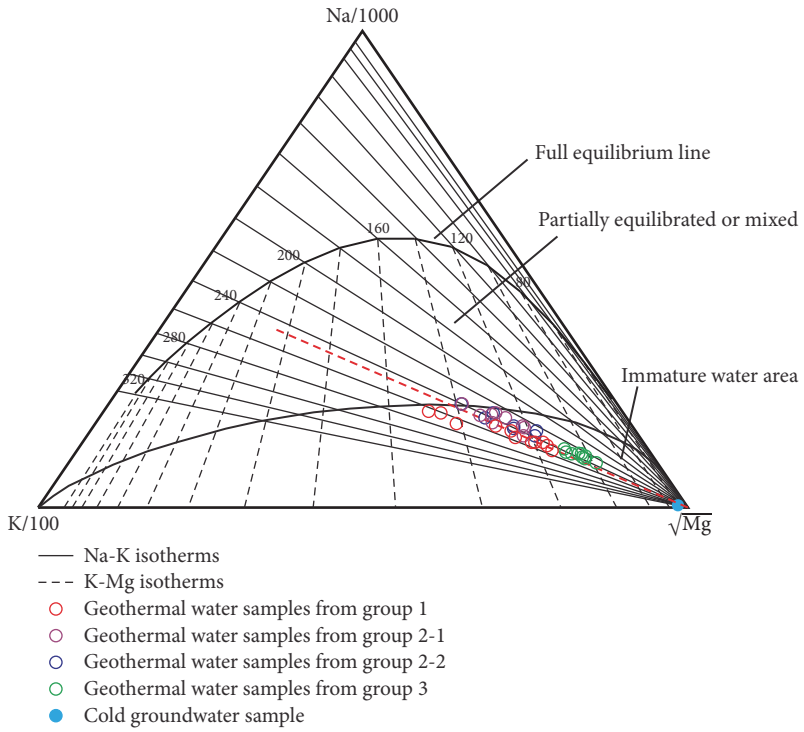

Figure 6: Na-K-Mg diagram for all the geothermal spring samples in the research area [15].

than those from the Na-K-Ca geothermometer, as the Ca contents of groups 2 and 3 are relatively higher, especially for the samples of subgroup 2-2 and group 3, where the Ca contents reach 10–23 mg/L. The Na-K-Ca geothermometer makes a correction for the Ca content of the water, thereby removing some ambiguity; thus, the results from the Na-K-Ca geothermometer for the Ca-rich samples of groups 2 and 3 could be adopted.

4.2.4. Silica-Enthalpy Mixing Model. In the silica-enthalpy mixing model, except for samples C3, C33, C34, and C35 from group 1, the extrapolations of the lines through other data points of the cold and emerging spring waters have no intersection point with the quartz solubility curve, indicating that most of the geothermal fluids in the research area have not mixed with shallow cooler water during ascent to the surface (Figure 7). Regarding the deep geothermal waters that are not mixed with shallow cooler water during ascent, the connection lines of the sampling points and the steam point are extended to intersect the quartz solubility curve at points B and C (the upper and lower limits). The corresponding temperatures of the geothermal reservoirs are 176–205°C; however, this method underestimated the temperatures of some geothermal samples from group 2 and group 3, as they are mainly cooled by conduction during ascent to the surface. The results calculated using the quartz geothermometer with no loss of steam and the Na-K-Ca geothermometer listed in Table 3 are more optimal.

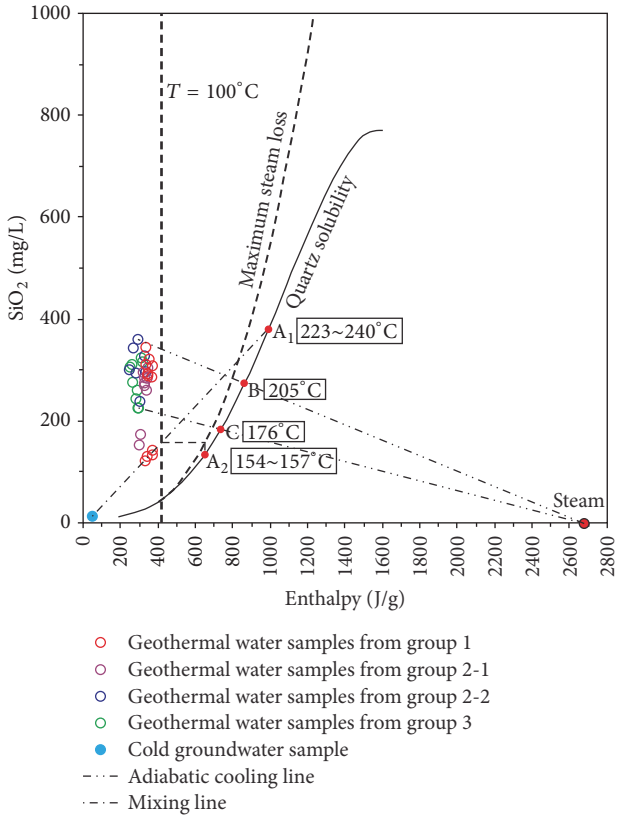

Figure 7: Silica-enthalpy mixing models of geothermal spring samples in the research area.

Table 3: Calculation results of geothermal reservoir temperatures in the research area (T in ˚C, except for mass flow rate in L/min). The results in bold font are the optimum temperatures selected from the quartz geothermometers taking into account the measured emerging temperatures and the mass flow rates of the spring samples.

Group	Sample ID	Emerging temperature	Mass flow rate	Quartz (maximum steam loss)	Quartz (no loss of steam)	Na-K-Ca	Na/K	K/Mg
1	C31	87.3	1842.6	**193.83**	211.80	235.20	240.51	126.90
	C34	87.2	1311.6	**152.31**	160.68	235.52	236.34	115.83
	C35	78.6	70.32	**142.98**	149.45	235.08	236.62	121.90
	C6	81.4	172.8	**190.67**	207.84	230.93	235.71	131.88
	C32	87	98.16	**189.34**	206.19	238.57	235.32	121.02
	C3	80.8	21.6	146.32	**153.46**	229.30	233.48	127.54
	C33	87.3	17.34	147.35	**154.70**	231.68	231.45	116.93
	C5	81.8	151.2	**189.79**	206.74	225.24	228.35	118.11
	C19	78.7	324	**194.34**	212.45	244.19	248.12	147.29
	C20	83.2	496.8	**196.27**	214.87	250.26	255.90	143.63
	C18	79.2	64.8	**200.74**	220.49	249.05	253.13	150.87
2-1	C1	70.4	-	153.95	**162.66**	211.32	216.33	127.67
	C26	76	-	**191.10**	208.39	210.78	217.46	122.57
	C23	81.6	-	**193.04**	210.81	211.57	214.96	122.73
	C36	77.6	432	**185.61**	201.54	211.98	216.20	130.49
	C11	80.6	216	**188.66**	205.34	214.87	220.28	131.90
	C25	77.2	-	**188.87**	205.59	219.03	232.32	132.47
	C4	72.2	0.216	160.59	**170.73**	227.19	230.56	123.75
	C21	77.4	-	**186.62**	202.78	213.01	224.59	140.15
	C7	80	-	**183.54**	198.95	219.72	229.37	135.64
2-2	C24	66	6.48	190.99	**208.25**	201.80	222.87	120.04
	C28	71	21.6	178.32	**192.49**	202.59	226.49	126.36
	C22	78.8	43.2	**191.42**	208.78	205.34	230.03	134.41
	C30	57.6	2.16	192.40	**210.01**	203.34	225.37	140.61
	C27	70	-	**203.80**	224.36	206.39	223.42	126.09
	C29	62.6	43.2	**200.55**	220.25	192.97	212.35	118.47
	C2	77.6	86.4	**197.62**	216.56	202.48	217.58	131.09
3	C14	70	2.16	175.32	**188.79**	197.54	221.06	96.58
	C16	66.2	21.6	179.47	**193.91**	198.74	214.06	104.61
	C15	62	2.16	187.00	**203.27**	198.03	224.27	108.92
	C8	67.8	2.16	183.62	**199.06**	195.72	216.99	99.59
	C12	68.8	21.6	175.02	**188.41**	204.12	220.91	104.22
	C9	58.8	21.6	193.37	**211.23**	199.40	221.49	105.18
	C17	61.4	21.6	194.35	**212.45**	207.46	226.81	110.94
	C13	74.6	32.4	**195.54**	213.95	193.66	213.81	103.10
	C10	73	-	**197.03**	215.82	198.43	218.39	106.32

For samples C3, C33, C34, and C35 from group 1, different intersections were provided by the two methods mentioned in "Materials and Methods" (Figure 7). If there is no steam separation before mixing, the intersection point A_1 provides the temperature range of 223–240˚C; however, if steam separation occurs before mixing, the intersection point A_2 lies within the temperature range of 154–157˚C. Obviously, the geothermal reservoir temperatures obtained at intersection point A_1 (223–240˚C) are more comparable to those calculated using the Na/K geothermometer. The mixing ratio of cold water with initial deep geothermal water could be calculated by dividing the distance of point A_1 to the cold water by that of point A_1 to the measured emerging water (Table 4).

Therefore, the results of the silica-enthalpy mixing model indicate that most of the geothermal fluids in the research area do not mix with shallow cooler water during ascent to the surface. A few samples from group 1 experience mixing

Table 4: Parameters of geothermal spring samples that experience mixing during ascent obtained from silica-enthalpy mixing models (T in ˚C).

Sample ID	Na/K	Maximum steam loss	No loss of steam	Mixture ratio of cold water (%)
C34	236.34	240.76	156.61	66.9
C35	236.62	232.68	154.71	69.7
C3	233.48	240.29	155.90	69.7
C33	231.45	227.21	154.23	64.8

during ascent and the mixture ratios of cold water with initial deep geothermal water are approximately 65%–70%. The temperatures of the geothermal reservoirs are approximately 223–240˚C with no steam separation before mixing, which are consistent with the corresponding Na/K results.

4.2.5. Selected Reservoir Temperatures. The calculated results from the K/Mg geothermometer for groups 1, 2, and 3 are 115.83–150.87˚C, 96.58–110.94˚C, and 118.47–140.61˚C, respectively, which are significantly lower than those of the quartz and Na/K (Na-K-Ca) results (Table 3). The system K-Mg approaches mineral-fluid equilibrium at low temperatures because of the obviously rapid response to variations in temperature, which reinforce the view that the subsurface geothermal fluids in the research area generally mix with cooler water in the reservoirs [46, 47].

The spring samples from group 1 and subgroup 2-1 fall significantly below the "equal temperature" line of Figure 8, especially for the samples from group 1, of which the results estimated from Na/K geothermometer are much higher than that from the quartz geothermometer. The Na/K (Na-K-Ca) results of group 1 and subgroup 2-1 are 228–256˚C and 215–232˚C. Except for a few samples that mixed with considerable amount of shallow cold water during ascent, the quartz results of group 1 and subgroup 2-1 are 189–201˚C and 184–193˚C, respectively. When initial temperatures are above approximately 210–230˚C, silica is likely to precipitate during ascent owing to relatively rapid rates of reaction at higher temperatures and the attainment of supersaturation with respect to amorphous silica as the solution cools. This silica precipitation may coat the channels and prevent other water–rock reactions, particularly those involving Na, K, and Ca. In this situation, the Na/K(Na-K-Ca) geothermometer could provide higher and more reliable results than those of the silica geothermometer [19, 48].

The quartz results of samples C3, C33, C34, and C35 are 143–155˚C, which are significantly lower than those of the other samples in the same group. According to the silica-enthalpy mixing models, the temperatures of deep initial fluids are consistent with the corresponding Na/K results, and the mixture ratios of cold water with initial deep geothermal water are approximately 65%–70%. Therefore, it can be speculated that, before significant precipitation of silica, these samples mixed with a considerable amount of shallow cold water during ascent leading to lower quartz results, which could be corrected using the silica-enthalpy mixing model.

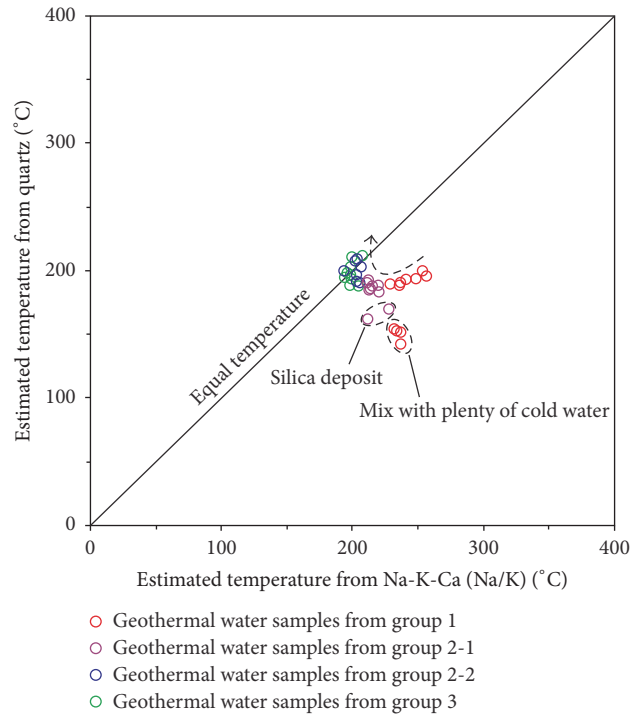

Figure 8: Comparison of geothermal reservoir temperatures estimated using quartz and Na/K (Na-K-Ca) geothermometers in the research area. Na/K results were applied to samples of group 1, and Na-K-Ca results were applied to samples of groups 2 and 3.

The quartz results of samples C1 and C4 from subgroup 2-1 are obviously lower than those of the other samples in the same group, while their Na-K-Ca temperatures are comparable to the others. The lower quartz results are a result of mixing with cold water as shown in the silica-enthalpy mixing models. The measured emerging temperatures and mass flow rates of these two samples are much lower than those of other samples in the same group, which indicate that they mainly experienced conductive cooling during ascent. Therefore, the lower SiO_2 contents are probably due to silica deposition in the case of high initial temperatures and relatively slower mass flow rates of the geothermal fluids.

The spring samples from group 3 and subgroup 2-2 plot near the "equal temperature" line. The results of the quartz geothermometer (188–212˚C) agree well with those of the Na-K-Ca geothermometer (193–207˚C), suggesting that the geothermal waters of group 3 and subgroup 2-2 reached a fluid–rock chemical equilibrium during ascent to the surface [15, 49]. Some samples plot slightly above the "equal temperature" line which might be a result of the effects of slight evaporation. Samples from group 3 and subgroup 2-2 generally featured low measured emerging temperatures, slow mass flow rates, and high TDS, indicating they mainly undergo conductive cooling during ascent to the surface (Figure 9). Therefore, both the quartz and Na-K-Ca geothermometers could provide reasonable temperatures of geothermal reservoirs.

In summary, for most samples from group 1 and subgroup 2-1, an Na/K or Na-K-Ca geothermometer could be used to

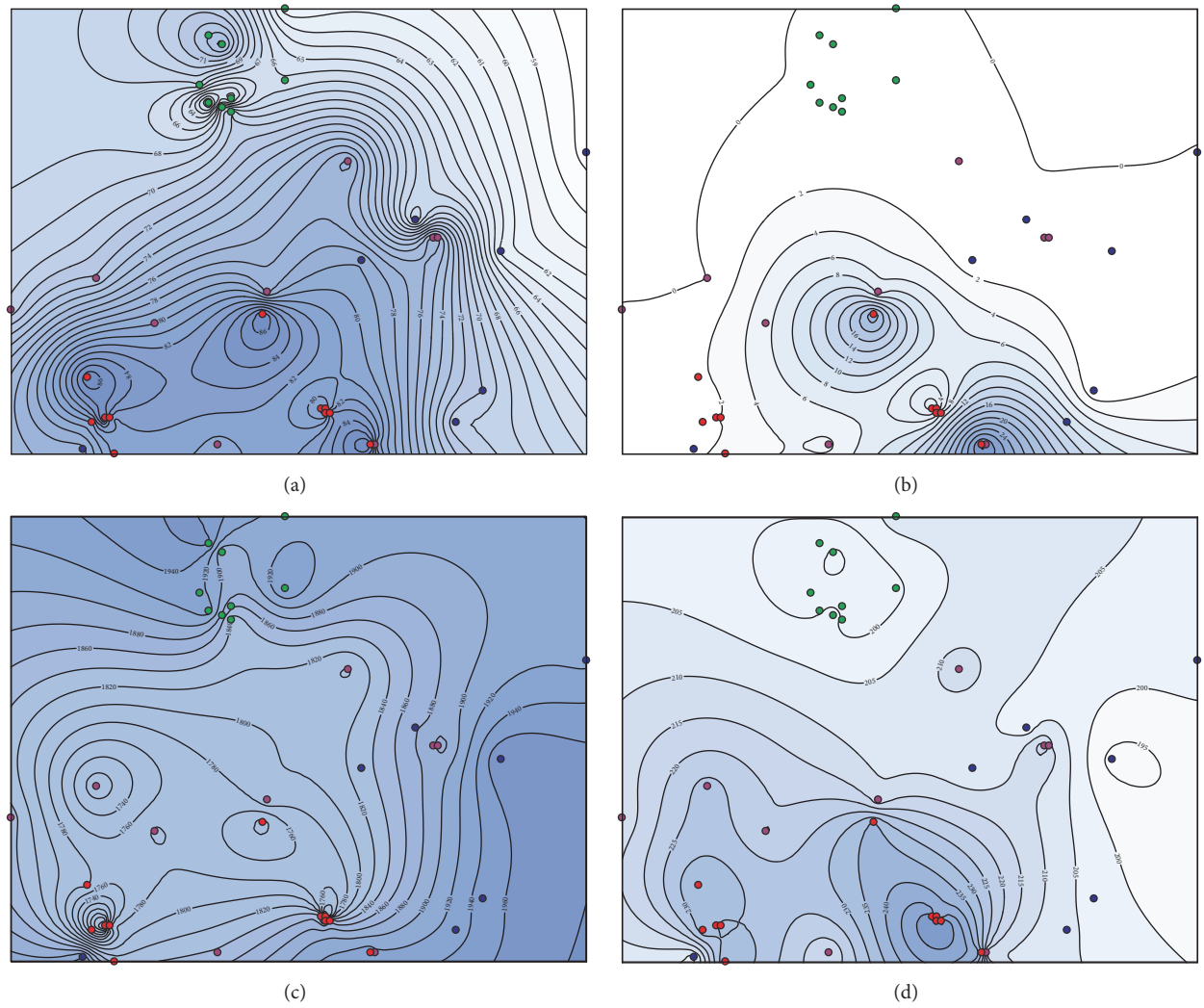

Figure 9: Contour maps of the geothermal spring samples in the research area. Figures 9(a), 9(b), and 9(c) are the contour maps of measured emerging temperatures, mass flow rates, and TDS of the spring samples, respectively; Figure 9(d) is the contour map of reasonable temperatures of geothermal reservoirs determined in "Selected Reservoir Temperatures."

estimate reasonable temperatures of geothermal reservoirs, while, for the samples from group 1 mixing with a considerable amount of shallow cold water during ascent, a silica-enthalpy plot could also be applied to obtain reasonable temperatures. For samples from group 3 and subgroup 2-2, both the quartz and Na-K-Ca geothermometers could provide reasonable results for the geothermal reservoirs.

4.3. Variation Characteristics of Geothermal Reservoir Temperatures. Contour maps were applied to measure emerging temperatures, mass flow rates, and TDS of the spring samples and the reasonable temperatures of geothermal reservoirs as determined in "Selected Reservoir Temperatures." This shows that the measured emerging temperatures and mass flow rates gradually decrease from the central part to the peripheral belt (Figures 9(a) and 9(b)), while the opposite change is found with TDS (Figure 9(c)). This indicates that, from the central part to the peripheral belt, the major cooling processes of the subsurface geothermal fluids gradually transform from adiabatic boiling to conduction. Figure 9(d) shows an increasing trend of geothermal reservoir temperatures from the center to the periphery. The point with the highest temperature (256°C) appears in the east-central part of the research area, of which the emerging temperature and mass flow rate are relatively high, and the TDS is obviously lower. Therefore, this point might be the main up-flow zone of the subsurface geothermal fluids.

On the whole, the measured emerging temperatures, mass flow rates, and TDS of the spring samples and the reasonable temperatures of geothermal reservoirs change regularly from the central part to the peripheral belt, which are consistent with the distribution of the sinter platform and are mainly controlled by the north-south trending fracture.

4.4. Cooling Process of Subsurface Geothermal Fluids. As shown in the piper diagram (Figure 5), the Na-K-Mg triangular plot (Figure 6), and contour maps (Figure 9), from

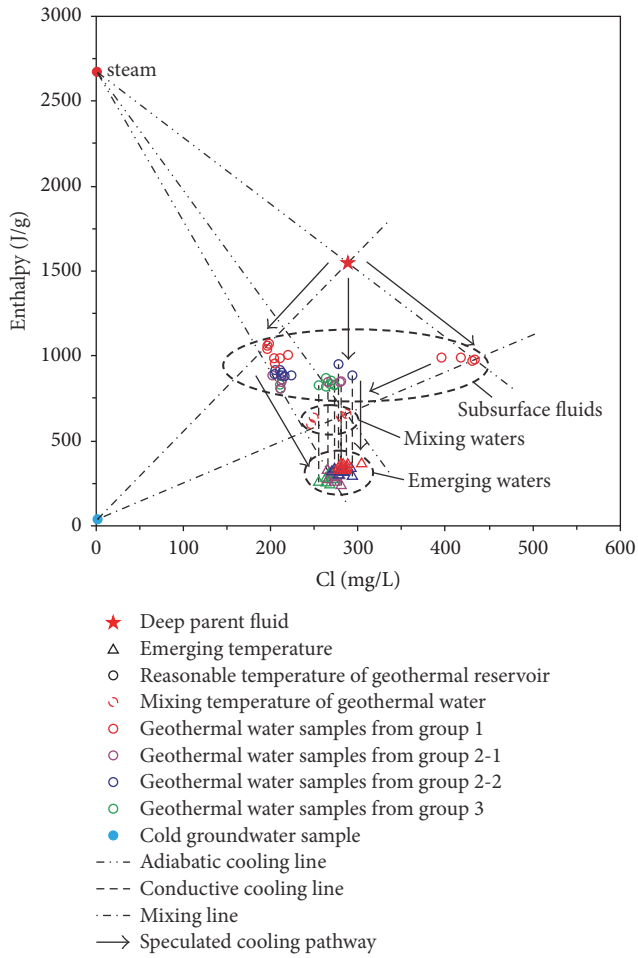

FIGURE 10: Enthalpy-chloride plot for the geothermal spring samples of the research area.

the central part (represented by group 1) to the peripheral belt (represented by group 3), the major cooling processes of the subsurface geothermal fluids gradually transform from adiabatic to conductive. Furthermore, most of the geothermal fluids in the research area do not mix with shallow cooler water during ascent to the surface, except for a few samples from group 1. Therefore, on the enthalpy-chloride plot of geothermal water samples from the research area (Figure 10), for most of the geothermal spring samples from group 1 and subgroup 2-1, an Na-K-Ca or Na/K geothermometer was used to estimate the subsurface temperatures. In addition, the results of the quartz geothermometers were used to represent mixing temperatures for the mixed samples from group 1, which could differentiate the various processes interfering with the evolution of deep fluids. For the geothermal spring samples from group 3 and subgroup 2-2, although both the quartz and Na-K-Ca geothermometers could provide reasonable temperatures of the geothermal reservoirs, the subsurface temperatures were uniformly provided by the Na-K-Ca geothermometer, as the cation geothermometer is barely affected by mixing with cold water or boiling.

The major cooling process of each sample was determined using the measured emerging temperature and the mass flow rate of the corresponding spring, just as the selection process of optimal temperature was estimated using quartz geothermometers. For samples that mainly experienced adiabatic cooling while ascending, straight lines were extended from the sampling points to S (the steam point at zero chloride), marking the enthalpies of the subsurface geothermal fluids along the corresponding lines to obtain the locations of subsurface geothermal fluids on the enthalpy-chloride plot. For the samples that are mainly cooled by conduction during ascent, their chloride contents generally will be nearly the same as that of the waters in the aquifers feeding the springs [18, 50, 51]. The reasonable temperatures of the geothermal reservoirs are plotted directly above the sampling points. For the samples from group 1 that mixed with a considerable amount of shallow colder water during ascent, their sampling and mixing temperatures were estimated using the quartz geothermometer, and they are used to mark the temporary points on the graph. Then, these points are connected to the cold groundwater point and combined with the Na/K temperatures to obtain the locations of subsurface geothermal fluids on the enthalpy-chloride plot.

According to the enthalpy-chloride plot, the deep parent fluid of the Chabu geothermal field is estimated to have a Cl^- concentration of 290 mg/L and an enthalpy of 1550 J/g (water temperature of 369°C). The deep parent fluid mainly experienced adiabatic boiling, conduction, or mixing with cooler water, to form the subsurface geothermal fluids in the reservoirs. Most of the subsurface geothermal fluids emerging on the surface as hot or boiling springs are mainly cooled by adiabatic boiling or conduction. In addition to adiabatic or conductive cooling, a few subsurface geothermal fluids mix with a considerable amount of shallow colder water during ascent and emerge with unsaturated quartz.

5. Conclusions

In this study, the geothermal spring samples were collected systematically from the north-central part of the sinter platform, which holds the most concentrated and intense hydrothermal manifestations in the Chabu high-temperature geothermal system. All the geothermal spring samples were divided into three groups (group 2 could be further divided into two subgroups) using cluster analysis of major elements. Samples of group 1 and group 3 were distributed in the central part and northern periphery of the sinter platform, respectively, while samples of group 2 were scattered in the transitional zone between groups 1 and 3. On the triangular plot of $Cl\text{-}SO_4\text{-}HCO_3 + CO_3$ and the Na-K-Mg diagram, a linear relationship of all the samples was presented, which was found to be the one main indicator of mixing between geothermal fluids and shallow cooler waters in the geothermal reservoirs. Furthermore, samples of groups 1, 2, and 3 draw near to cold groundwater, indicating that there is a gradually increasing mixture of geothermal waters and shallow cooler water from group 1 to group 2 to group 3.

The optimal quartz temperature of each sample was selected by considering the measured emerging temperature and the mass flow rate of the corresponding spring. Then, the reasonable reservoir temperatures and the mixing processes

of the subsurface geothermal fluids in the research area were defined by combining the calculated results of the quartz and cation geothermometers with the silica-enthalpy mixing models. For most samples from group 1 and subgroup 2-1, the Na/K or Na-K-Ca geothermometer could be used to estimate reasonable reservoir temperatures, as silica is likely to precipitate during ascent owing to relatively rapid rates of reaction at high temperatures (>210°C). For the samples from group 1 mixing with shallow cold water during ascent, a silica-enthalpy plot could also be applied to obtain reasonable reservoir temperatures. For samples from group 3 and subgroup 2-2, both the quartz and Na-K-Ca geothermometers could provide reasonable results for the geothermal reservoirs. Contour maps were applied to measure emerging temperatures, mass flow rates, and TDS of the spring samples and reasonable reservoir temperatures. These indicated that, from the central part to the peripheral belt, the major cooling processes of the subsurface geothermal fluids gradually transform from adiabatic boiling to conduction. These also showed an increasing trend of geothermal reservoir temperatures from the center to the periphery. The point with the highest temperature (256°C) appears in the east-central part of the research area, which might be the main up-flow zone for the subsurface geothermal fluids.

The cooling processes of the subsurface geothermal fluids in the research area can be shown on an enthalpy-chloride plot. The deep parent fluid for the Chabu geothermal field has a Cl^- concentration of 290 mg/L and an enthalpy of 1550 J/g (water temperature of 369°C). The deep parent fluid ascends to high-temperature geothermal reservoirs and forms subsurface geothermal fluids mainly cooled by adiabatic boiling, conduction, or mixing with cooler water. Most of the subsurface geothermal fluids emerging on the surface as hot or boiling springs are mainly cooled by conduction or adiabatic cooling, though some fraction of the geothermal waters mixed with a considerable amount of shallow colder water during ascent and emerged with unsaturated quartz.

Conflicts of Interest

The authors declare that they have no conflicts of interest.

Acknowledgments

This work was financially supported by the Basal Research Fund from the Institute of Hydrogeology and Environmental Geology, Chinese Academy of Geological Sciences (no. SK201501, no. SK201606) and the National Natural Science Foundation of China (no. 41672249, no. 41502249). The manuscript benefited from numerous constructive comments by Nvdawa and Chuanlu.

References

[1] P. Tapponnier and P. Molnar, "Active faulting and tectonics in China," *Journal of Geophysical Research: Atmospheres*, vol. 82, no. 20, pp. 2905–2930, 1977.

[2] Z. Q. Hou and Z. Q. Li, "Possible location for underthrusting front of the Indus continent: constraints from helium isotope of the geothermal gas in southern Tibet and eastern Tibet," *Acta Geologica Sinica*, vol. 78, no. 4, pp. 482–493, 2004 (Chinese).

[3] Z. Q. Li, Z. Q. Hou, F. J. Nie, and X. J. Meng, "Characteristic and distribution of the partial melting layers in the upper crust: evidence from active hydrothermal fluid in south Tibet," *Acta Geologica Sinica*, vol. 79, no. 1, pp. 68–76, 2005 (Chinese).

[4] L. D. Brown, W. Zhao, K. D. Nelson et al., "Bright spots, structure, and magmatism in southern Tibet from INDEPTH seismic reflection profiling," *Science*, vol. 274, no. 5293, pp. 1688–1690, 1996.

[5] P. Zhao, J. Jin, H. Z. Zhang, J. Duo, and T. Liang, "Chemical composition of thermal water in the Yangbajing geothermal field, Tibet," *Scientia Geologica Sinica*, vol. 33, no. 1, pp. 61–72, 1998 (Chinese).

[6] L. Hoke, S. Lamb, D. R. Hilton, and R. J. Poreda, "Southern limit of mantle-derived geothermal helium emissions in Tibet: Implications for lithospheric structure," *Earth and Planetary Science Letters*, vol. 180, no. 3-4, pp. 297–308, 2000.

[7] Z. Q. Hou, Z. Q. Li, X. M. Qu et al., "Qinghai-Tibet plateau uplift process since 0.5 Ma—evidence from hydrothermal activity of Gangdise belt," *Science in China Series D*, vol. 44, no. S1, pp. 35–44, 2001 (Chinese).

[8] P. Zhao, E. J. Xie, J. Dor et al., "Geochemical characteristics of geothermal gases and their geological implications in Tibet," *Acta Petrologica Sinica*, vol. 18, no. 4, pp. 539–550, 2002 (Chinese).

[9] J. A. Becker, M. J. Bickle, A. Galy, and T. J. B. Holland, "Himalayan metamorphic CO_2 fluxes: quantitative constraints from hydrothermal springs," *Earth and Planetary Science Letters*, vol. 265, no. 3-4, pp. 616–629, 2008.

[10] W. Zhao, P. Kumar, J. Mechie et al., "Tibetan plate overriding the Asian plate in central and northern Tibet," *Nature Geoscience*, vol. 4, no. 12, pp. 870–873, 2011.

[11] Q. Guo, "Hydrogeochemistry of high-temperature geothermal systems in China: A review," *Applied Geochemistry*, vol. 27, no. 10, pp. 1887–1898, 2012.

[12] Q. Guo, D. K. Nordstrom, and R. B. McCleskey, "Towards understanding the puzzling lack of acid geothermal springs in Tibet (China): insight from a comparison with Yellowstone (USA) and some active volcanic hydrothermal systems," *Journal of Volcanology and Geothermal Research*, vol. 288, pp. 94–104, 2014.

[13] Z. Liu, W. Lin, M. Zhang, E. Xie, Z. Liu, and G. Wang, "Geothermal fluid genesis and mantle fluids contributions in Nimu-Naqu, Tibet," *Earth Science Frontiers*, vol. 21, no. 6, pp. 356–371, 2014 (Chinese).

[14] P. Stelling, L. Shevenell, N. Hinz, M. Coolbaugh, G. Melosh, and W. Cumming, "Geothermal systems in volcanic arcs: Volcanic characteristics and surface manifestations as indicators of geothermal potential and favorability worldwide," *Journal of Volcanology and Geothermal Research*, vol. 324, pp. 57–72, 2016.

[15] W. F. Giggenbach, "Geothermal solute equilibria. Derivation of Na-K-Mg-Ca geoindicators," *Geochimica et Cosmochimica Acta*, vol. 52, no. 12, pp. 2749–2765, 1988.

[16] M. Afsin, D. M. Allen, D. Kirste, U. G. Durukan, A. Gurel, and O. Oruc, "Mixing processes in hydrothermal spring systems and implications for interpreting geochemical data: A case study in the Cappadocia region of Turkey," *Hydrogeology Journal*, vol. 22, no. 1, pp. 7–23, 2014.

[17] J. X. Li, Q. H. Guo, and Y. X. Wang, "Evaluation of temperature of parent geothermal fluid and its cooling processes during

ascent to surface: a case study in Rehai geothermal field, Tengchong," *Earth Science*, vol. 40, no. 9, pp. 1576–1584, 2015 (Chinese).

[18] R. O. Fournier, "Chemical geothermometers and mixing models for geothermal systems," *Geothermics*, vol. 5, pp. 41–50, 1977.

[19] R. O. Fournier, "Geochemical and hydrologic considerations and the use of enthalpy-chloride diagrams in the prediction of underground conditions in hot-spring systems," *Journal of Volcanology and Geothermal Research*, vol. 5, no. 1-2, pp. 1–16, 1979.

[20] M. P. Asta, M. J. Gimeno, L. F. Auqué, J. Gómez, P. Acero, and P. Lapuente, "Hydrochemistry and geothermometrical modeling of low-temperature Panticosa geothermal system (Spain)," *Journal of Volcanology and Geothermal Research*, vol. 235-236, pp. 84–95, 2012.

[21] Ö. Avşar, N. Güleç, and M. Parlaktuna, "Hydrogeochemical characterization and conceptual modeling of the Edremit geothermal field (NW Turkey)," *Journal of Volcanology and Geothermal Research*, vol. 262, pp. 68–79, 2013.

[22] Z. M. Zhang, X. Dong, M. Santosh, and G. C. Zhao, "Metamorphism and tectonic evolution of the Lhasa terrane, Central Tibet," *Gondwana Research*, vol. 25, no. 1, pp. 170–189, 2014.

[23] T. L. Han, *Evolution on the Lithospheric Deformation of the Himalayan: Tibetan Active Tectonics*, 1987 (Chinese), Geological Publishing House.

[24] Y. Y. Zhao, X. T. Zhao, and Z. B. Ma, "Study on chronology for hot spring typed Cs-deposit of Targjia, Tibet," *Acta Petrologica Sinica*, vol. 22, no. 3, pp. 717–724, 2006 (Chinese).

[25] D. K. Nordstrom, J. W. Ball, R. J. Donahoe, and D. Whittemore, "Groundwater chemistry and water-rock interactions at Stripa," *Geochimica et Cosmochimica Acta*, vol. 53, no. 8, pp. 1727–1740, 1989.

[26] E. Dotsika, D. Poutoukis, and B. Raco, "Fluid geochemistry of the Methana Peninsula and Loutraki geothermal area, Greece," *Journal of Geochemical Exploration*, vol. 104, no. 3, pp. 97–104, 2010.

[27] M. Blasco, L. F. Auqué, M. J. Gimeno, P. Acero, and M. P. Asta, "Geochemistry, geothermometry and influence of the concentration of mobile elements in the chemical characteristics of carbonate-evaporitic thermal systems. The case of the Tiermas geothermal system (Spain)," *Chemical Geology*, vol. 466, pp. 696–709, 2017.

[28] J. Wang, R. Zuo, and J. Caers, "Discovering geochemical patterns by factor-based cluster analysis," *Journal of Geochemical Exploration*, vol. 181, pp. 106–115, 2017.

[29] Y.-H. Kao, S.-W. Wang, S. K. Maji et al., "Hydrochemical, mineralogical and isotopic investigation of arsenic distribution and mobilization in the Guandu wetland of Taiwan," *Journal of Hydrology*, vol. 498, pp. 274–286, 2013.

[30] J. C. Davis, *Statistics and Data Analysis in Geology*, John Wiley & Sons, Inc., New York, NY, USA, 2nd edition, 1990.

[31] L. S. Kalkstein, G. Tan, and J. A. Skindlov, "An evaluation of three clustering procedures for use in synoptic climatological classification," *Journal of Climate and Applied Meteorology*, vol. 26, no. 6, pp. 717–730, 1987.

[32] M. Zou, B. Yu, J. Cai, and P. Xu, "Fractal model for thermal contact conductance," *Journal of Heat Transfer*, vol. 130, no. 10, Article ID 101301, 9 pages, 2008.

[33] A. H. Truesdell and R. O. Fournier, "Procedure for estimating the temperature of a hot-water component in a mixed water by using a plot of dissolved silica versus enthalpy," *Journal of Research of the U. S. Geological Survey*, vol. 5, no. 1, pp. 49–52, 1977.

[34] Q. Guo, Z. Pang, Y. Wang, and J. Tian, "Fluid geochemistry and geothermometry applications of the Kangding high-temperature geothermal system in eastern Himalayas," *Applied Geochemistry*, vol. 81, pp. 63–75, 2017.

[35] M. Burgos, "Geothermal interpretation of thermal fluid discharge from wells and springs in Berlin Geothermal Field, EI Salvador," *The United Nations University Reports*, vol. 7, no. 7, pp. 165–191, 1999.

[36] W. Wagner and H. J. Kretzschmar, *International Steam Tables, Properties of Water and Steam Based on the Industrial Formulation IAPWS-IF97*, Springer-Verlag, Berlin, Germany, 2nd edition, 2008.

[37] R. O. Fournier, "Application of water geochemistry to geothermal exploration and reservoir engineering," in *Geothermal Systems: Principles and Case Histories*, pp. 109–143, John Wiley and Sons, New York, NY, USA, 1981.

[38] H. Saibi and S. Ehara, "Temperature and chemical changes in the fluids of the Obama geothermal field (SW Japan) in response to field utilization," *Geothermics*, vol. 39, no. 3, pp. 228–241, 2010.

[39] G. Schettler, H. Oberhänsli, G. Stulina, and J. H. Djumanov, "Hydrochemical water evolution in the Aral Sea Basin. Part II: confined groundwater of the Amu Darya Delta—evolution from the headwaters to the delta and SiO_2 geothermometry," *Journal of Hydrology*, vol. 495, pp. 285–303, 2013.

[40] S. Arnórsson, "Chemical equilibria in icelandic geothermal systems-Implications for chemical geothermometry investigations," *Geothermics*, vol. 12, no. 2-3, pp. 119–128, 1983.

[41] R. O. Fournier and A. H. Truesdell, "Chemical indicators of subsurface temperature applied to hot spring waters of Yellowstone National Park, Wyoming, U.S.A.," *Geothermics*, vol. 2, no. 1, pp. 529–535, 1970.

[42] J. Duo, "The basic characteristics of the Yangbajing geothermal field—a typical high temperature geothermal system," *Engineering Science*, vol. 5, pp. 42–47, 2003 (Chinese).

[43] H. L. Sun, F. Ma, W. Lin, Z. Liu, G. Wang, and D. Nan, "Geochemical characteristics and geothermometer application in high temperature geothermal field in Tibet," *Geological Science and Technology Information*, vol. 3, pp. 171–177, 2015 (Chinese).

[44] R. O. Fournier and A. H. Truesdell, "Geochemical indicators of subsurface temperature-part 2, estimation of temperature and fraction of hot water mixed with cold water," *Journal of Research of the U. S. Geological Survey*, vol. 2, pp. 263–270, 1974.

[45] R. O. Fournier and A. H. Truesdell, "An empirical NaKCa geothermometer for natural waters," *Geochimica et Cosmochimica Acta*, vol. 37, no. 5, pp. 1255–1275, 1973.

[46] N. Majumdar, A. L. Mukherjee, and R. K. Majumdar, "Mixing hydrology and chemical equilibria in Bakreswar geothermal area, Eastern India," *Journal of Volcanology and Geothermal Research*, vol. 183, no. 3-4, pp. 201–212, 2009.

[47] Y. Liu, X. Zhou, Z. Deng et al., "Hydrochemical characteristics and genesis analysis of the Jifei hot spring in Yunnan, southwestern China," *Geothermics*, vol. 53, pp. 38–45, 2015.

[48] S. Arnórsson, "The use of mixing models and chemical geothermometers for estimating underground temperatures in geothermal systems," *Journal of Volcanology and Geothermal Research*, vol. 23, no. 3-4, pp. 299–335, 1985.

[49] S. Chatterjee, S. Sharma, M. A. Ansari et al., "Characterization of subsurface processes estimation of reservoir temperature in

Tural Rajwadi geothermal fields, Maharashtra, India," *Geothermics*, vol. 59, pp. 77–89, 2016.

[50] M. R. Carvalho, V. H. Forjaz, and C. Almeida, "Chemical composition of deep hydrothermal fluids in the Ribeira Grande geothermal field (São Miguel, Azores)," *Journal of Volcanology and Geothermal Research*, vol. 156, no. 1-2, pp. 116–134, 2006.

[51] T. Özen, A. Bülbül, and G. Tarcan, "Reservoir and hydrogeochemical characterizations of geothermal fields in Salihli, Turkey," *Journal of Asian Earth Sciences*, vol. 60, pp. 1–17, 2012.